ACS Photonics

Article

pubs.acs.org/journal/apchd5

Gold Nanoantennas on a Pedestal for Plasmonic Enhancement in the Infrared

Christian Huck,[†] Andrea Toma,[‡] Frank Neubrech,[†,§] Manohar Chirumamilla,[‡] Jochen Vogt,[†] Francesco De Angelis,[‡] and Annemarie Pucci*[,†]

[†]Kirchhoff Institute for Physics, University of Heidelberg, Im Neuenheimer Feld 227, 69120 Heidelberg, Germany

[‡]Istituto Italiano di Tecnologia, Via Morego 30, 16163 Genova, Italy

[§]4th Physics Institute and Research Center SCoPE, University of Stuttgart, Pfaffenwaldring 57, 70569 Stuttgart, Germany

Supporting Information

ABSTRACT: The coupling of an infrared plasmon-polariton excitation of a metal nanoparticle to a vibrational excitation of a similar energy enables strong vibrational signal enhancement. However, the commonly used planar substrates substantially weaken plasmonic resonances because of their polarizability, and, furthermore, a great part of the enhanced near-field is inside the substrate and thus not available for an analyte. In this contribution we report on a way to reduce these undesirable influences of the substrate by fabricating gold nanowires on high pedestals and thus in reduced contact with the substrate. The influence of the height of the pedestal is an important parameter for the plasmonic near-field enhancement, as we show with finite-difference time-domain simulations. Comparing the plasmonic response and the SEIRA activity of the rods prepared by standard electron beam lithography and the rods additionally treated with reactive ion etching to remove the silicon substrate at the hot-spots of the rods reveals not only the change of the plasmonic-resonance spectrum but also interesting differences of the enhanced phonon-polariton signal from the silicon dioxide layer on the silicon substrate and the about 1 order of magnitude stronger vibrational signal enhancement for an adsorbate monolayer.

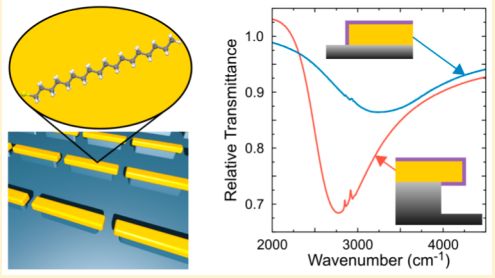

KEYWORDS: *infrared, plasmonics, optical nanoantennas, reactive ion etching, surface-enhanced infrared absorption, SEIRA*

In recent years, metal nanoparticles have attracted tremendous interest in the field of nano-optics because the excitation of plasmon-polaritons in the nanoparticles leads to strong electromagnetic field confinements with an intensity that can be more than 3 orders of magnitude higher than that of the incoming light. These extraordinarily high electromagnetic fields can be exploited for sensing applications such as surface-enhanced fluorescence,[1,2] surface-enhanced infrared absorption (SEIRA),[3−8] and surface-enhanced Raman spectroscopy (SERS).[9−12] SEIRA, for example, is a versatile tool for the detection of biological, medical, or chemical analytes that are located around metallic nanostructures at very low concentration. One great advantage of SEIRA compared to other, unspecific sensing techniques, such as refractive index sensing, is its capability to provide molecular information on the analyte due to material-specific vibrational absorptions in the IR-fingerprint region.[13−15] The near-field of a nanostructure and therefore the vibrational signal enhancement depend on several properties such as the shape of the nanostructure,[16] the coupling to other nanostructures, and also the supporting substrate. So the near-field coupling of two[17] or more[18] nanostructures with nanometer-sized separations provides an even higher electromagnetic near-field and therefore a higher sensitivity. The polarizability of the supporting substrate strongly influences the plasmonic activity of the nanostructures. Nanostructures prepared on substrates with high refractive indices, such as silicon or zinc sulfide, feature a lower extinction cross-section, lower near-field enhancements, and a red-shifted resonance position compared to low refractive index substrates such as glass or calcium fluoride.[19−21] One approach to keep the chemical stability of, for example, silicon and to simultaneously take advantage of a low refractive index is the use of elevated nanostructures, which are only partially influenced by the substrate. Such structures can be prepared for example by wet etching[22] or reactive ion etching (RIE).[23,24] They have already shown promising results, for example, the increase of SERS sensitivity by more than 1 order of magnitude,[23−25] of the refractometric localized surface plasmon resonance (LSPR) sensing,[26−29] and of SEIRA.[22] The use of elevated nanostructures additionally allows the preparation of reconfigurable nanoantennas using electron beam manipulation,[30] as recently shown.

For SEIRA, the pedestal not only lowers the polarizability effect from the substrate but also brings about more near-field sites for the analyte.[22] With the spatial extent of vibrational signal enhancement up to 100 nm[31] it is desirable to have pedestals of at least this height. There is a further advantage of

Received: October 8, 2014
Published: March 26, 2015

DOI: 10.1021/ph500374r
ACS Photonics 2015, 2, 497−505

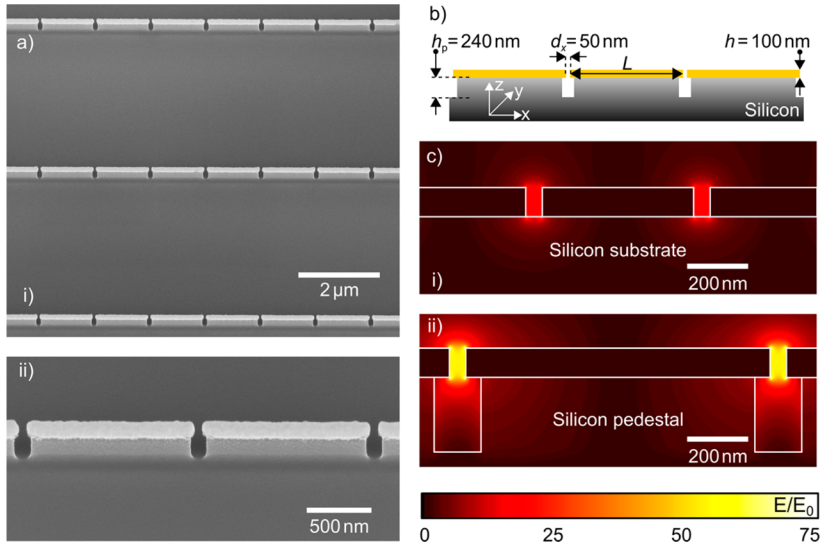

Figure 1. (a) SEM images: overview (i) and zoom-in (ii) recorded under an angle of 45 deg of gold nanoantennas on a silicon substrate elevated by RIE. The side view shows the silicon pedestal with a height of approximately 240 nm and the gold nanoantenna on top. (b) Schematic illustration depicting the sample layout used in the numerical calculations. (c) Near-field distribution of resonantly excited nanoantennas situated directly on top of the substrate (i) and nanoantennas elevated by silicon pedestals (ii). The antenna lengths L have been adjusted in such a way that both arrays have the same resonance frequency. The simulated near-field distribution is recorded at a plane normal to the y-direction.

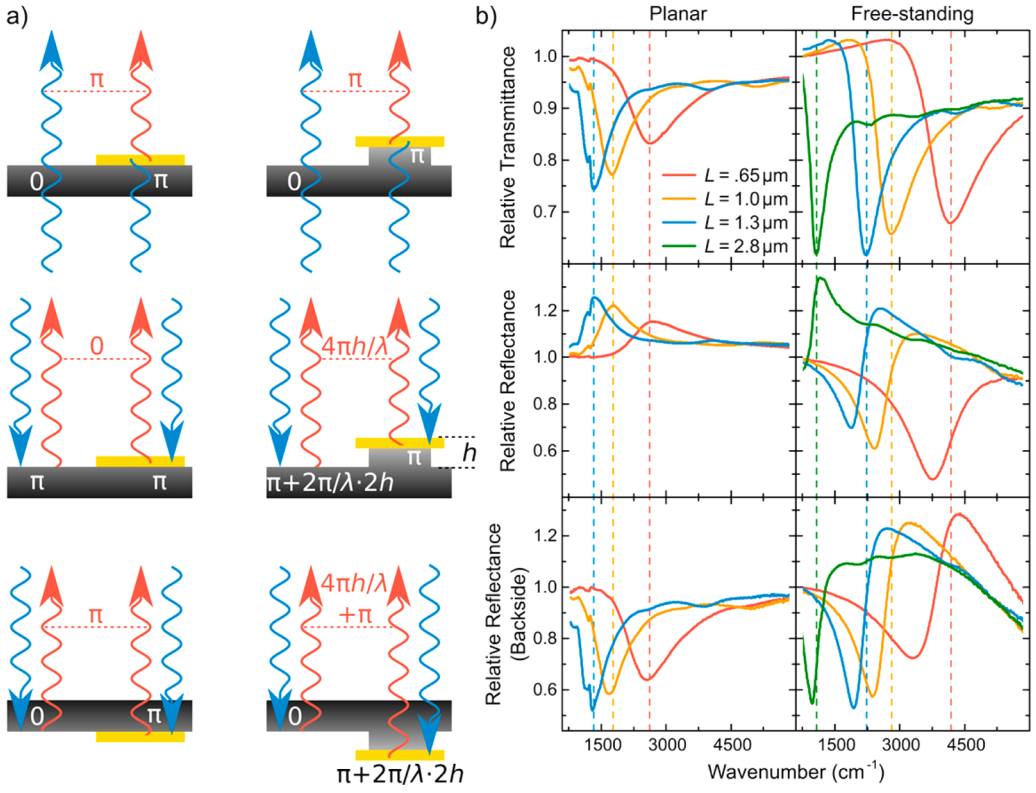

Figure 2. Relative transmittance, relative reflectance, and relative reflectance from the backside of planar and free-standing gold nanoantennas. (a) Schematic representation of the measurement geometries. Incoming light is partially reflected/transmitted by the substrate and thus partially interacts with a nanoantenna, resulting in, among others, a phase shift of π at the resonance frequency. The pedestal of the nanoantenna leads to a difference in path length and therefore to an additional phase shift. The induced phase shift at the resonance frequency of the nanoantenna combined with the phase shift due to the difference in path length is given in the figure. The final phase relation between light reflected/transmitted by the substrate and light scattered by the nanoantenna at the resonance frequency is given in red. (b) Measured spectra: For planar structures, transmittance, reflectance, and backside reflectance peak at the same frequency, e.g., the resonance frequency (marked with dashed vertical lines), whereas for the free-standing nanoantennas the phase shift introduced by the pedestal leads to a shift of the minimum/maximum in reflectance. Since the phase shift induced by the difference in path length is wavelength dependent, the resultant spectra show parts where the reflectance is increased and parts where it is decreased.

DOI: 10.1021/ph500374r
ACS Photonics 2015, 2, 497−505

such height, as we will show here. For high-reflecting substrates and sufficiently high pedestals, interferences may further increase the near-field enhancement and thus produce an even stronger SEIRA signal intensity. We investigated the benefit of free-standing gold nanoantennas on silicon substrates for a series of SEIRA measurements and discuss their plasmonic properties in various measurement geometries. Elevated gold nanoantennas were prepared by electron beam lithography (EBL) and subsequent RIE, which allows a very high etching depth with the resultant nanostructures being very stable. We demonstrate changes in the plasmonic line shape in relation to the measurement geometry for planar and free-standing nanoantennas and explain the results within a simplified model of two interfering beams. The influence of the substrate is monitored as the shift of the resonance frequency due to the change of refractive index and as the modified enhancement of vibrational excitations of the native silicon dioxide (SiO_2) layer and of a self-assembled monolayer (SAM) of octadecanethiol (ODT).

RESULTS AND DISCUSSION

To experimentally investigate the influence of the substrate on the plasmonic properties and, further, the intensities of SEIRA signals, two identical samples containing nanoantenna arrays with different lengths have been prepared by EBL on silicon substrates (see Methods). In a second step one of the two samples has been treated by RIE (see Methods) to remove the upper layers of the silicon substrate. This method allows an undercut of the nanostructures, resulting in gold nanoantennas on top of a silicon pedestal (see Figure 1b). The height of the pedestal can be adjusted by the etching time and was set to 240 nm, which was confirmed by atomic force microscopy measurements. Subsequent to the preparation the sample has been inspected with scanning electron microscopy (SEM) (see Figure 1a). The upper image shows an overview of the sample and the lower image a zoom to two nanoantennas. The images were taken under an angle of 45° with respect to normal incidence. The SEM images shows that the nanoantennas are elevated from the substrate over a silicon pedestal. The influence of the substrate on the near-field distribution has been investigated by FDTD calculations (see Methods). Figure 1c shows the near-field distributions of a planar and a free-standing nanoantenna array. Both distributions are shown at the resonance frequency (ω_{res}) that is similar for both cases. Corresponding far-field spectra are shown in the Supporting Information (Figure S3). The point with the highest field enhancement for the planar structure is inside the substrate and therefore not accessible for sensing applications, such as SEIRA. In contrast, the hot-spot of the free-standing nanoantennas is completely accessible, and additionally the amplitude is much higher due to the reduced substrate effects.

After sample preparation planar and free-standing nanoantennas were investigated by micro-IR spectroscopy (see Methods) in different excitation geometries. Figure 2b shows typical IR spectra, whereas in Figure 2a the corresponding measurement geometry is schematically depicted. In transmittance geometry both samples behave in a similar way: At the resonance of the nanoantennas transmittance is lowered, since light is absorbed and scattered by the nanoantenna. Resonantly scattered light in the forward direction can interfere destructively with IR light not modified by the nanoantennas because light scattered by the nanoantennas is phase-shifted by π. The resonance frequency of the planar nanoantennas is much lower compared to that of free-standing nanoantennas, since the RIE removal of the silicon lowers the effective refractive index around the nanoantennas. Apart from a spectral blue-shift, decreasing the surrounding refractive index leads to a higher extinction.[21] Besides the shift of the resonance curve and the different extinction, the line shape of the planar and the free-standing sample does not differ much in the transmittance geometry. However, the line shape in the reflectance geometry (middle panel of Figure 2b) is totally different for the free-standing nanoantennas. The planar design shows an IR response as usual in reflectance geometry: At the far-field resonance frequency (frequency with the lowest transmittance) the reflectance is highest, since light is scattered back from the nanostructures. Far apart from the resonance the reflectance goes back to 100% because the sample reflects the same amount of light as the reference (bare silicon substrate). In contrast, the free-standing nanoantennas, *e.g.*, with a length of 1 μm (orange curve), show a reflectance of less than 100% for frequencies below the resonance frequency and a value above 100% for higher ones. To explain this behavior, one has to consider not only the light scattered by the nanoantennas but also the light reflected by the substrate, which is schematically shown in Figure 2a. If light is reflected at the medium with the higher refractive index, its phase is shifted by π. Additional to this phase shift, the light has to travel a longer distance compared to light interacting with the nanoantennas because the nanoantennas are elevated from the substrate. This difference in path length leads to an additional phase shift that adds up to $\Delta\phi_S = \pi + 2\pi/\lambda \times 2h$. The phase shift induced by the nanoantenna is $\Delta\phi_A = \pi$ at the resonance frequency, smaller than π for frequencies below the resonance frequency and bigger than π for frequencies above the resonance frequency. The total phase shift between light reflected by the substrate and light scattered by the nanoantennas at the resonance frequency therefore is $\Delta\phi = \Delta\phi_S - \Delta\phi_A = 4\pi h/\lambda_{res}$ and is dependent on the resonant wavelength. For resonance wavelengths larger than the pedestal height ($\lambda_{res} \gg h$, green curve in Figure 2b) $\Delta\phi$ gets small, and therefore the two light beams interfere constructively, like in the planar case ($h = 0$), leading to an increase in reflectance. However, if the resonant wavelength approaches values close to $h = \lambda_{res}/4$, the overall phase shift becomes $\Delta\phi = \pi$ and the two light beams interfere destructively, resulting in a decrease in reflectance (red curve in Figure 2b). In between $0 < h < \lambda_{res}/4$ light interferes partially constructively and destructively, respectively, and therefore the reflectance at the resonance frequency shows neither a minimum nor a maximum. In these cases the minimum in reflectance is always well below the resonance frequency found in transmittance, because the overall phase shift $\Delta\phi$ increases for frequencies below the resonance frequency (see Supporting Information). By turning the sample upside down (lower panel of Figure 2), two things change: First, the light reflected at the substrate/air interface is not phase shifted by π anymore, because now the light is reflected at the medium with the lower refractive index. For the planar sample this results in a flip of all resonance curves, meaning that the reflectance has its minimum at the resonance frequency. Second, the difference in path length changes the sign because now the path of light reflected by the substrate is the shorter one. The latter affects only the free-standing nanoantennas. These changes lead to an overall phase shift of $\Delta\phi = \Delta\phi_S - \Delta\phi_A = \pi + 4\pi h/\lambda_{res}$. For large resonance wavelengths, the free-standing nanoantennas again behave similar to the planar ones because the pedestal height is

DOI: 10.1021/ph500374r
ACS Photonics 2015, 2, 497−505

small compared to the wavelength ($\lambda_{res} \gg h$). However, the spectra are not just flipped like in the planar case. Instead, the minimum in reflectance is again always at frequencies lower than the resonance frequency for the same reason as discussed for the normal reflectance. A more detailed description of the model, as well as a fit to the measurement data, is shown in the Supporting Information.

As could be seen, by partially removing the silicon substrate the resonance frequency of the nanoantennas is strongly blue-shifted. Figure 3 shows the resonant wavelength's dependence

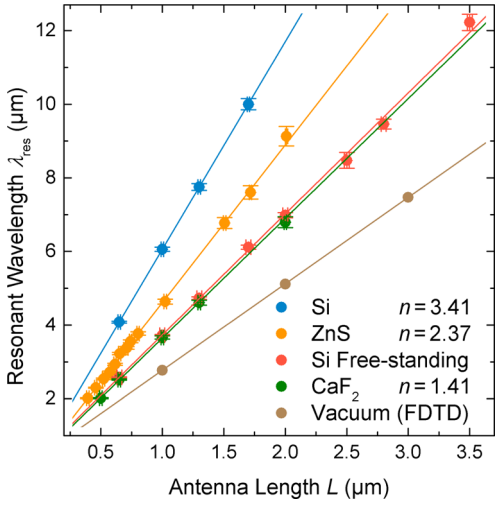

Figure 3. Resonance wavelength λ_{res} versus antenna length L for gold nanoantennas with similar dimensions on various substrates. A high refractive index substrate such as silicon leads to a steep slope. By treating the silicon substrate with reactive ion etching the slope can be decreased down to the value of CaF_2, which has a relatively low refractive index of n = 1.41. For comparison the resonance wavelength−antenna length relation is also shown for nanoantennas supported by zinc sulfide substrates and surrounded by vacuum (FDTD simulations).

on the antenna length L for gold nanoantennas with similar dimensions on various substrates. A high refractive index substrate such as silicon (n = 3.41) leads to a steep increase of the resonant wavelength of a nanoantenna. By removing the silicon substrate with reactive ion etching the slope can be decreased down to the value of CaF_2 that has a relatively low refractive index of n = 3.41. For comparison also the data for a ZnS substrate and without a substrate (antenna in a vacuum) are shown. The vacuum line results from a numerical calculation and gives the minimum slope that can be achieved.

Usually, to describe the effect of the substrate on IR spectra of metal nanoparticles, a rough approximation of the effective dielectric constant $\varepsilon_{eff} = (n_S^2 + n_{Air}^2)/2$ is assumed[32,33] as embedding the particle completely (n_S and n_{Air} are the refractive indices of the substrate and air). Figure 3 shows that the substrate influence of the free-standing nanoantennas on the silicon substrate is similar to the influence of a CaF_2 substrate on antennas lying directly on the substrate, which means that the effective refractive index in both cases is very similar. This allows a rough estimation of the amount of silicon in the vicinity of the free-standing antennas. With ε_{eff} from above we thus assume $\varepsilon_{eff,CaF2} = (n_{CaF2}^2 + n_{Air}^2)/2 = x \times n_{Si}^2 + (1-x) \times n_{Air}^2 = \varepsilon_{eff,Si}$. Solving this equation for x with n_{CaF2} = 1.41, n_{Air} = 1, and n_{Si} = 3.41 we get x = 4.6%. This x-value means that the RIE approach reduced the substrate effect from 50% down to 4.6%, and so the "hot-spots" are indeed free of silicon. In total, the advantages of silicon substrates, e.g., the chemical stability and the broad spectral transmittance window (1−20 μm), can be combined with the advantages of a low refractive index substrate, e.g., the higher near-field enhancement (see Figure 1c), the bigger structure size that is easier to fabricate, and a good compatibility with electronic devices. Additionally, the volume of the hot-spots that is accessible for sensing applications is bigger than for planar antennas, where the hot-spots are partly located inside the substrate.

The influence of the pedestal height (h_p) on the near-field intensity was investigated by means of finite-difference time-domain (FDTD) simulations and is shown in Figure 4. The

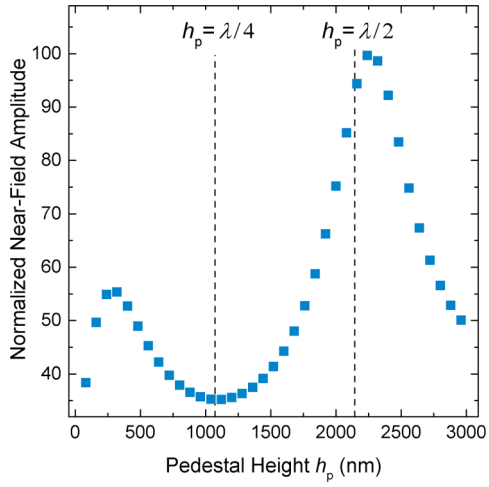

Figure 4. Calculated near-field amplitude at the resonance position of nanoantennas with a length of L = 1000 nm for varying pedestal height h_p evaluated in the middle of the gap. The development shows the characteristics of a nanocavity resonance: The near-field amplitude is maximal if half of the resonance wavelength of the nanoantenna matches the pedestal height and is minimal if the pedestal height is a quarter of the resonance wavelength.

figure shows the near-field amplitude in the middle of the 50 nm gap at the resonance frequency of a nanoantenna array with an antenna length of L = 1000 nm. The near-field amplitude increases until a pedestal height of approximately h_p = 250 nm, then decreases again and has its minimum if h_p is equal to a quarter of the wavelength. For higher values of h_p the near-field amplitude increases again until $h_p = \lambda/2$. This behavior can be explained as a resonance of a cavity that has every half wavelength the standing wave resonance along the cavity length.[24] Therefore, the near-field amplitude has its maximum if the nanocavity is resonant at the same frequency as the nanoantennas, what happens if half of the resonant wavelength of the nanoantennas matches the pedestal height. If the pedestal height is a quarter of the wavelength, the cavity effect lowers the near-field amplitude. This case also describes the system with the lowest reflectance, as it was explained in Figure 2. The drop down of the near-field amplitude for pedestal heights smaller than 250 nm is explained by the increased influence of the substrate on the nanoantenna, as discussed before. For an optimization of the geometry with respect to the SEIRA enhancement, the pedestal height has to be adjusted to the maximum near-field. By following this approach, the near-field enhancement is more than doubled compared to a planar nanoantenna (see also Figure 1c). Since SEIRA scales with the

DOI: 10.1021/ph500374r
ACS Photonics 2015, 2, 497−505

near-field intensity, the expected signal size is more than 4 times higher.

In order to demonstrate the benefit of free-standing antennas for SEIRA, two different vibrational systems were investigated and compared to SEIRA studies using planar antennas. First, we consider the vibrational signal enhancement of a thin (3 nm) native SiO_2 layer beneath the metal nanostructures[34] that allows the excitation of phonon-polaritons on a planar surface[35] under normal incidence of light. For the planar antennas, the whole substrate is covered with a uniform SiO_2 layer (see inset of Figure 5). The SiO_2 layer of the free-standing antennas was

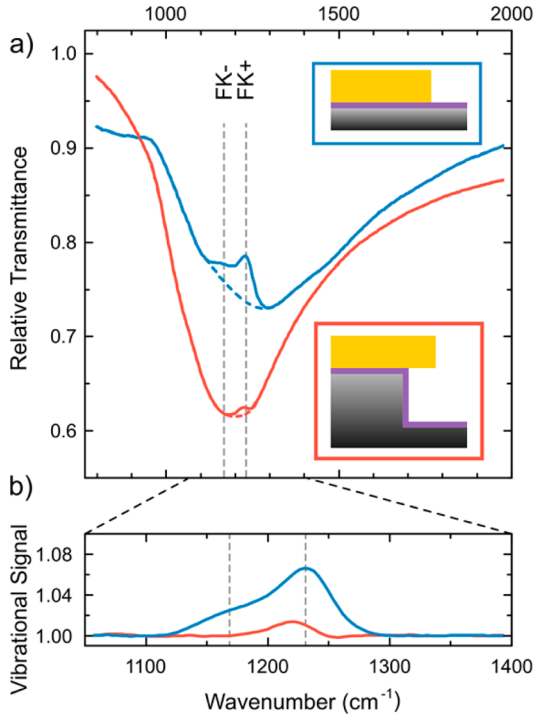

Figure 5. (a) Transmittance spectra of the nanostructures on SiO_2/Si and (b) vibrational (transmittance) signals of SiO_2 phonon-polaritons after the baseline correction: For the planar antennas (L = 1300 nm) the enhanced SiO_2-phonon excitation is clearly visible, whereas for the free-standing antennas (L = 2500 nm) the phonon-polariton excitation is only marginally enhanced, since the SiO_2 layer has a bigger distance to the hot-spots of the nanoantennas. The SiO_2 layer is indicated in purple in the schematic in the inset of the figure. The positions of the Fuchs–Kliewer (FK+ and FK–) excitations as attributed to the two observed vibrational features are marked with dashed vertical lines.

removed during the RIE process with the exception of the SiO_2 directly on the pedestal beneath the nanoantennas. However, the native SiO_2 layer on the planar substrate surface spontaneously re-forms when the sample is exposed to air. Therefore, in our measurements, the substrate and the silicon pedestal side planes are also covered with SiO_2 (see inset of Figure 5).

Figure 5a compares measurements of planar and free-standing nanoantennas with lengths of L = 1300 nm for the planar antennas and L = 2500 nm for the free-standing ones. Due to the different resonance wavelength–length relation (see Figure 3), both arrays are resonant at ω_{res} = 1200 cm^{-1}, which is the frequency range of the phonon-polariton excitation. Considering both the interfaces (Si/SiO_2 and SiO_2/Air), two types of surface phonon-polariton excitations on the planar SiO_2 layer are possible, known as Fuchs–Kliewer (FK) modes.[36,37] The phonon-polariton that propagates at the interface Si/SiO_2 (FK–) is influenced by the substrate dielectric function and has lower frequencies than the phonon-polariton located at the surface (FK+). In order to evaluate the enhanced phononic signals, both samples were baseline corrected by dividing the baseline given by the plasmonic resonance (dashed line in Figure 5a; see ref 17 for details). The resultant vibrational signal is shown in Figure 5b. The sample with the planar nanoantennas shows a broad peak that can be attributed to the two phonon-polariton excitations.[38] The plasmonic line shape is strongly modified by the SiO_2 oscillators. In contrast, for the free-standing nanoantennas only a very weak signal (see Figure 5b) at the FK + frequency can be observed and the plasmonic line shape is only marginally influenced. The much stronger vibrational signal for the planar antennas can be explained by the distribution of the electromagnetic near-field enhancement that has its highest value inside the substrate, close to the interface (see Figure 1c). Therefore, the electric field inside the SiO_2 layer is very pronounced, which leads to a strong coupling to the phonon-polariton excitations, even stronger than observed in ref 34. The coupling of the free-standing antennas that show a much higher electromagnetic near-field, however, is very weak, because the field enhancement is almost outside the SiO_2 layer. The hot-spot is mainly located around the tip ends of the antennas, which is more than 200 nm away from the planar SiO_2 layer, and also any oxide on the pedestal does not give any important SEIRA contribution in the range of the Si–O stretching reststrahl band.

The second vibrational system we investigated is a monolayer of ODT. ODT features four different vibrational normal modes in the range between 2800 and 3000 cm^{-1} belonging to the symmetric and antisymmetric stretching vibration of the methyl and the methylene groups.[7] Since the molecule consists of only one methyl group compared to 17 methylene groups, the two vibrations belonging to the methylene groups are much more prominent compared to the two vibrations of the methyl group. The samples were cleaned with piranha solution and oxygen plasma, and a SAM of ODT was formed (see Methods). Subsequently, the antenna arrays with the resonance frequency matching the ODT vibrations (antenna length L = 1000 nm for free-standing and L = 650 nm for planar antennas) were measured with IR microspectroscopy (Figure 6). The signal intensity of an enhanced vibrational signal strongly depends on the tuning between the resonance frequency and the frequency of the molecular vibrations.[38] Therefore, different lengths have been used with the objective to achieve a good match for the free-standing as well as the planar antennas. Nevertheless the resonance frequency of the planar nanoantenna does not perfectly match the vibrational frequency; a quantitative comparison for both the sample types is still possible (notice that the electromagnetic near-field maximum is shifted to lower frequencies compared to the far-field maximum):[39,40] The planar array shows only very weak vibrational signals from the stretching vibration of the methylene groups. But the sample with the elevated nanostructures shows much higher signals, and all four ODT vibrational modes can be distinguished. The increased signal intensity with the use of the free-standing nanoantennas proves the increased sensing area and the increased electromagnetic near-field intensity. The surface area of a nanoantenna that is available for the ODT adsorption is increased due to two facts: First, after RIE, the area on the bottom side of a nanoantenna is also partly available for ODT

DOI: 10.1021/ph500374r
ACS Photonics 2015, 2, 497–505

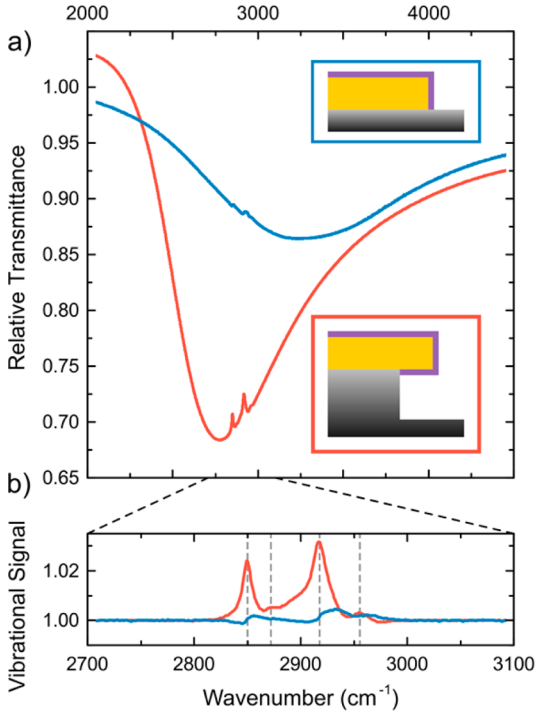

Figure 6. (a) Relative IR transmittance in the spectral region of the fundamental resonance of a planar and a free-standing gold nanoantenna array with antenna lengths of L = 650 nm and L = 1000 nm, respectively, covered with one-monolayer ODT. The sensing area covered with ODT is indicated in purple in the schematics in the insets of the figure. (b) Baseline-corrected vibrational (transmittance) signal of the symmetric and asymmetric CH_2 and CH_3 vibrations (vertical dashed lines). Much larger signals are found for the free-standing antennas.

adsorption, and second, the length of the free-standing nanoantenna can nearly be doubled compared to the planar one with the same resonance frequency. Table 1 compares the

Table 1. Comparison of the Sensing Area, Integrated Near-Field Intensity, and Vibrational Signal of the ODT Layers[a]

	sensing area per antenna (μm^2)	integrated near-field intensity I/I_0 per antenna ($\times 10^3$ nm^3)	enhanced vibrational signal of $\nu(CH_2)_s$
free-standing nanoantennas	0.49	44.3	0.024
planar nanoantennas	0.24	4.5	0.003

[a]The enhanced vibrational signals were determined by using the peak-to-peak value of the baseline-corrected Fano-type signal of the CH_2 stretching vibration ($\nu(CH_2)_s$) in the transmittance spectrum at 2855 cm^{-1}, shown in Figure 6b.

sensing area per nanoantenna, the integrated near-field intensity per nanoantenna, and the measured ODT signal size of both samples. The near-field intensity has been calculated by integrating the electromagnetic field intensity over the volume where the ODT adsorbs (purple volume in the inset of Figure 6). The vibrational signal size of the ODT has been calculated by dividing the measured spectrum by a baseline that was determined iteratively with an algorithm proposed by Eilers[41] (see ref 17 for further details) and using the peak-to-peak value of the vibrational signal of that baseline-corrected spectrum (shown in Figure 6b). It turns out that the sensing area is approximately doubled whereas the integrated near-field intensity is 10 times higher for the free-standing nanoantennas. The integrated near-field intensity for the free-standing antennas is higher than that of the planar nanoantennas because for the latter a non-negligible part of the electromagnetic field is inside the substrate and therefore not accessible for sensing applications and, more important, the much lower near-field intensity of the hot-spots (see Figure 1c and Figure 4). For a comparison with the measurement data one has additionally to take into account the number of antennas involved in the measurement, which is a factor of 1.5 higher for the planar antennas, due to their shorter length. Considering this, the integrated near-field intensity over the whole measurement spot of the free-standing antennas is a factor of 6.7 bigger, which is in good agreement with the ratio of the measured enhanced vibrational signals (7.6) shown in the last column of Table 1.

SUMMARY AND CONCLUSION

We explained the RIE-based preparation and showed the benefit of gold nanoantennas on a specially nanostructured substrate for surface-enhanced infrared spectroscopy. We investigated the IR plasmonic response in different measurement geometries and explained the resultant line shape within a simple interference model for the role of the pedestal height. The influence of the pedestal height on the near-field enhancement was investigated using FDTD calculations, which show the highest electromagnetic near-field amplitude if the pedestal height is equal to half of the resonance wavelength, but they show already a maximum at the pedestal height achieved in this work. The decreased influence of the underlying substrate leads to a tremendous blue-shift of the measured resonance frequencies, which is in accord with the lowered refractive index of the surroundings of the nanoantennas. Also the decreased phononic signals of the SiO_2 surface layer on the silicon substrate are related to the much weaker near-field intensity inside the SiO_2 layer because of the distance provided by the silicon pedestal. Due to the blue-shift of the plasmonic resonance frequency, the length of the nanostructures can be increased approximately by a factor of 2, which increases the surface area available for molecular adsorption. The advantages of the elevated nanostructures for sensing applications were shown by enhanced vibrational spectroscopy of ODT test molecules. The peak-to-peak value of the vibrational features like the signal size could be increased by nearly 1 order of magnitude compared to the planar nanostructures, as quantitatively confirmed by numerical calculations.

METHODS

Gold Nanoantenna Fabrication. Free-standing (3D) gold nanoantennas were fabricated through the combination of EBL (Raith 150-Two) and RIE (SENTECH). A 250 nm thick layer of poly(methyl methacrylate) (PMMA, MicroChem Corp., 950 K) was spin-coated at 2000 rpm for 60 s onto a high-resistivity (>10 kΩcm) (100)-oriented silicon substrate. The sample was baked at 180 °C for 8 min in order to get uniform film thickness. To prevent charging effects during the electron exposure, a 10 nm thick Al layer was thermally evaporated on the PMMA surface. Electron beam direct-writing of the nanoantenna patterns was carried out at 20 kV accelerating

DOI: 10.1021/ph500374r
ACS Photonics 2015, 2, 497−505

voltage, 500 $\mu C/cm^2$ exposure dose, and 35 pA beam current. After the Al removal in a KOH solution, the exposed resist was developed in a conventional solution of methyl isobutyl ketone (MIBK) and isopropyl alcohol (IPA) of 1:3 mixture ratio at 12 °C for 60 s. Then, electron beam evaporation (Kurt J. Lesker system) was employed to produce layers of Ti and Au of 3 and 100 nm, respectively. An additional 50 nm chromium film was deposited by thermal evaporation in order to create an etch mask for the RIE process. The unexposed resist was removed with acetone and rinsed out in IPA. A mixture of gases, SF_6 (30 sccm) and C_4F_8 (32 sccm), was used to etch the silicon substrate. The pressure, temperature, and power were 1 mTorr, 5 °C, and 18 W, respectively, leading to an etch rate of 100 nm/min. Finally, the chromium layer was removed by dipping the sample in a standard Chrome Etch 18 solution (OSC OrganoSpezialChemie GmbH, Bitterfeld, Germany) for 40 s and rinsed in deionized water for 1 min. The composition of free-standing nanoantennas has been confirmed through energy-dispersive X-ray spectroscopy, which confirmed the presence of gold on the nanostructures and the absence of chromium residues (see Supporting Information). All SEM images were taken with a FEI Helios Nano lab 650.

The fabricated arrays consist of nanoantennas with a height of h = 100 nm, a width of w = 150 nm, and different lengths between 650 and 3500 nm and have been arranged with a longitudinal distance of d_x = 50 nm, a transverse separation of d_y = 5 μm, and a pedestal height of h_p = 240 nm (see Figure 1b). The height of the nanoantennas including the height of the silicon pedestal has been confirmed (h = 339 nm) by atomic force microscopy.

Binding of Octadecanethiol to Nanoantennas. As a model system for enhanced vibrational spectroscopy a self-assembled monolayer of alkanethiols was used. Subsequent to the preparation and characterization of the nanoantenna arrays, the planar and free-standing antennas were cleaned with piranha solution (H_2SO_4/H_2O_2 = 5:2) for 20 s to remove any sulfur contaminations from the RIE process. Additionally both samples were treated with oxygen plasma at 150 W for 10 min. In the following steps the samples were exposed to a 1 mmol solution of ODT (Sigma-Aldrich, 98%) in ethanol for at least 24 h,[42] carefully rinsed with pure ethanol to remove any unbound ODT molecules, and dried with a stream of nitrogen. ODT forms an almost homogeneous layer with a thickness of 2.8 nm.[43] It features various IR-active vibrational modes between 2800 and 3000 cm^{-1}, dominated by the symmetric and antisymmetric stretching vibration of the methyl (CH_3) and the methylene (CH_2) groups.

IR Extinction and SEIRA Spectroscopy. Infrared spectra were taken using IR radiation from a thermal light source. The measurements were performed with an IR microscope (Bruker Hyperion 1000) coupled to an FTIR spectrometer (Bruker Tensor 27). To reduce atmospheric IR absorption of water vapor and CO_2, the whole beam path was purged with dry air. Light was detected using a liquid-N_2-cooled mercury cadmium telluride detector. A polarizer was inserted in the optical path before the sample to polarize the light linearly with the electrical field vector along the long axis of the antennas. The nanoantenna arrays were located by means of white light microscopy, and an aperture with a diameter of 50 μm was placed in their center. In case of the measurements with the nanoantenna arrays located at the bottom-side of the substrate the array position was determined by measuring the distance to the substrate edges, and optimization of the IR response by systematically varying the position in 5 μm steps. Normal IR spectra were recorded with a resolution of 8 cm^{-1} and 200 scans. SEIRA spectra including the narrow band ODT vibrations were recorded with a resolution of 2 cm^{-1} and 3000 scans. As a reference, the bare silicon substrate was used for all measurements.

Numerical Simulations. Near-field distributions of the electromagnetic field have been calculated using the commercial 3D finite-difference time-domain software Lumerical FDTD-Solutions v8.7.3. The near-field distribution of nanoantenna arrays was obtained by numerically solving Maxwell's equations under normal incidence of infrared radiation polarized parallel to the long antenna axis. In a first approximation the silicon substrate was modeled dispersionless with a refractive index of n = 3.41 and the dielectric function of gold was described by a Drude model employing parameters for gold on silicon from ref 44 (e.g., plasma frequency ω_p = 67 900 cm^{-1}, scattering rate ω_τ = 384 cm^{-1}, dielectric background ε_∞ = 7.0). Periodic boundary conditions were used in the directions parallel to the substrate to get the response of an antenna array. In the direction perpendicular to the substrate perfectly matched layers (PMLs) were used to define the boundaries of the simulation volume. The nanoantennas were placed directly on the substrate or on a pedestal (see Figure 1b) with a distance to the PML of at least one wavelength in each direction. To resolve the geometry of the nanoantennas, with dimensions much smaller than the wavelength, subgridding techniques were used with a mesh size of 1 × 1 × 1 nm. The default grid of the simulation region outside the nanoantennas including the silicon pedestal is defined by the auto nonuniform mesh algorithm with a mesh accuracy of 4. The arrays were illuminated with a broadband (1500−3500 cm^{-1}) plane wave coming from the substrate direction, and the electromagnetic field was recorded with a 3D field profile monitor. Convergence testing was performed by increasing the simulation volume in the z-direction, the number of PMLs, and the simulation time and decreasing the mesh size. To further reduce the computational resources, all symmetries provided by the nanoantenna arrays were included in the simulation setup (e.g., symmetric boundaries in the transverse direction and antisymmetric boundaries in the longitudinal direction). All simulations were performed taking advantage of the high-performance cluster bwGRiD.

■ ASSOCIATED CONTENT

Supporting Information

Further information on the interference model, fit results to the measurement data, the influence of the pedestal height on the reflectance line shape, energy-dispersive X-ray spectroscopy results, discussion of collective phenomena, and the influence of the adhesion layer. This material is available free of charge via the Internet at http://pubs.acs.org.

■ AUTHOR INFORMATION

Corresponding Author

*Address correspondence to pucci@kip.uni-heidelberg.de.

Notes

The authors declare no competing financial interest.

■ ACKNOWLEDGMENTS

Financial support by the European project NANOANTENNA (HEALTH-F5-2009-241818) is gratefully acknowledged by the

DOI: 10.1021/ph500374r
ACS Photonics 2015, 2, 497−505

authors from the Kirchhoff-Institute for Physics and by the Italian Institute of Technology. C.H. acknowledges financial support by the Helmholtz Graduate School for Hadron and Ion Research. C.H. and J.V. acknowledge financial support by the Heidelberg Graduate School of Fundamental Physics. F.N. thanks the BW-Stiftung (PROTEINSENS) and the ERC (COMPLEXPLAS) for financial support. We are grateful for computational resources provided by the bwGRiD of the federal state of Baden-Wuerttemberg, Germany.

REFERENCES

(1) Bardhan, R.; Grady, N. K.; Cole, J. R.; Joshi, A.; Halas, N. J. Fluorescence Enhancement by Au Nanostructures: Nanoshells and Nanorods. *ACS Nano* **2009**, *3*, 744−752.
(2) Kinkhabwala, A.; Yu, Z.; Fan, S.; Avlasevich, Y.; Müllen, K.; Moerner, W. E. Large Single-Molecule Fluorescence Enhancements Produced by a Bowtie Nanoantenna. *Nat. Photonics* **2009**, *3*, 654−657.
(3) Cubukcu, E.; Zhang, S.; Park, Y.-S.; Bartal, G.; Zhang, X. Split Ring Resonator Sensors for Infrared Detection of Single Molecular Monolayers. *Appl. Phys. Lett.* **2009**, *95*, 043113.
(4) Aouani, H.; Šípová, H.; Rahmani, M.; Navarro-Cia, M.; Hegnerová, K.; Homola, J.; Hong, M.; Maier, S. A. Ultrasensitive Broadband Probing of Molecular Vibrational Modes with Multifrequency Optical Antennas. *ACS Nano* **2013**, *7*, 669−675.
(5) Cataldo, S.; Zhao, J.; Neubrech, F.; Frank, B.; Zhang, C.; Braun, P. V.; Giessen, H. Hole-Mask Colloidal Nanolithography for Large-Area Low-Cost Metamaterials and Antenna-Assisted Surface-Enhanced Infrared Absorption Substrates. *ACS Nano* **2012**, *6*, 979−985.
(6) D'Andrea, C.; Bochterle, J.; Toma, A.; Huck, C.; Neubrech, F.; Messina, E.; Fazio, B.; Maragò, O. M.; Di Fabrizio, E.; Lamy de La Chapelle, M.; Gucciardi, P. G.; Pucci, A. Optical Nanoantennas for Multiband Surface-Enhanced Infrared and Raman Spectroscopy. *ACS Nano* **2013**, *7*, 3522−3531.
(7) Neubrech, F.; Pucci, A.; Cornelius, T. W.; Karim, S.; Garcá-Etxarri, A.; Aizpurua, J. Resonant Plasmonic and Vibrational Coupling in a Tailored Nanoantenna for Infrared Detection. *Phys. Rev. Lett.* **2008**, *101*, 157403.
(8) Bagheri, S.; Giessen, H.; Neubrech, F. Large-Area Antenna-Assisted SEIRA Substrates by Laser Interference Lithography. *Adv. Opt. Mater.* **2014**, *2*, 1050−1056.
(9) Kneipp, K.; Wang, Y.; Kneipp, H.; Perelman, L. T.; Itzkan, I.; Dasari, R. R.; Feld, M. S. Single Molecule Detection Using Surface-Enhanced Raman Scattering (SERS). *Phys. Rev. Lett.* **1997**, *78*, 1667−1670.
(10) Theiss, J.; Pavaskar, P.; Echternach, P. M.; Muller, R. E.; Cronin, S. B. Plasmonic Nanoparticle Arrays with Nanometer Separation for High-Performance SERS Substrates. *Nano Lett.* **2010**, *10*, 2749−2754.
(11) Nie, S.; Emory, S. R. Probing Single Molecules and Single Nanoparticles by Surface-Enhanced Raman Scattering. *Science* **1997**, *275*, 1102−1106.
(12) Fazio, B.; D'Andrea, C.; Bonaccorso, F.; Irrera, A.; Calogero, G.; Vasi, C.; Gucciardi, P. G.; Allegrini, M.; Toma, A.; Chiappe, D.; Martella, C.; De Mongeot, F. B. Re-radiation Enhancement in Polarized Surface-Enhanced Resonant Raman Scattering of Randomly Oriented Molecules on Self-Organized Gold Nanowires. *ACS Nano* **2011**, *5*, 5945−5956.
(13) Adato, R.; Yanik, A. A.; Amsden, J. J.; Kaplan, D. L.; Omenetto, F. G.; Hong, M. K.; Erramilli, S.; Altug, H. Ultra-Sensitive Vibrational Spectroscopy of Protein Monolayers with Plasmonic Nanoantenna Arrays. *Proc. Natl. Acad. Sci. U.S.A.* **2009**, *106*, 19227−19232.
(14) Wu, C.; Khanikaev, A. B.; Adato, R.; Arju, N.; Yanik, A. A.; Altug, H.; Shvets, G. Fano-Resonant Asymmetric Metamaterials for Ultrasensitive Spectroscopy and Identification of Molecular Monolayers. *Nat. Mater.* **2012**, *11*, 69−75.
(15) Adato, R.; Altug, H. In-Situ Ultra-Sensitive Infrared Absorption Spectroscopy of Biomolecule Interactions in Real Time with Plasmonic Nanoantennas. *Nat. Commun.* **2013**, *4*, 2154.
(16) Kern, A. M.; Martin, O. J. F. Excitation and Reemission of Molecules near Realistic Plasmonic Nanostructures. *Nano Lett.* **2011**, *11*, 482−487.
(17) Huck, C.; Neubrech, F.; Vogt, J.; Toma, A.; Gerbert, D.; Katzmann, J.; Härtling, T.; Pucci, A. Surface-Enhanced Infrared Spectroscopy Using Nanometer-Sized Gaps. *ACS Nano* **2014**, *8*, 4908−4914.
(18) Brown, L. V.; Zhao, K.; King, N.; Sobhani, H.; Nordlander, P.; Halas, N. J. Surface-Enhanced Infrared Absorption Using Individual Cross Antennas Tailored to Chemical Moieties. *J. Am. Chem. Soc.* **2013**, *135*, 3688−3695.
(19) Valamanesh, M.; Borensztein, Y.; Langlois, C.; Lacaze, E. Substrate Effect on the Plasmon Resonance of Supported Flat Silver Nanoparticles. *J. Phys. Chem. C* **2011**, *115*, 2914−2922.
(20) Curry, A.; Nusz, G.; Chilkoti, A.; Wax, A. Substrate Effect on Refractive Index Dependence of Plasmon Resonance for Individual Silver Nanoparticles Observed Using Darkfield Micro-Spectroscopy. *Opt. Express* **2005**, *13*, 2668−2677.
(21) Fernández-García, R.; Sonnefraud, Y.; Fernández-Domínguez, A. I.; Giannini, V.; Maier, S. A. Design Considerations for Near-Field Enhancement in Optical Antennas. *Contemp. Phys.* **2014**, *55*, 1−11.
(22) Cetin, A. E.; Etezadi, D.; Altug, H. Accessible Nearfields by Nanoantennas on Nanopedestals for Ultrasensitive Vibrational Spectroscopy. *Adv. Opt. Mater.* **2014**, *2*, 866−872.
(23) Chirumamilla, M.; Toma, A.; Gopalakrishnan, A.; Das, G.; Zaccaria, R. P.; Krahne, R.; Rondanina, E.; Leoncini, M.; Liberale, C.; De Angelis, F.; Di Fabrizio, E. 3D Nanostar Dimers with a Sub-10-nm Gap for Single-/Few-Molecule Surface-Enhanced Raman Scattering. *Adv. Mater.* **2014**, *26*, 2353−2358.
(24) Hatab, N. A.; Hsueh, C.-H.; Gaddis, A. L.; Retterer, S. T.; Li, J.-H.; Eres, G.; Zhang, Z.; Gu, B. Free-Standing Optical Gold Bowtie Nanoantenna with Variable Gap Size for Enhanced Raman Spectroscopy. *Nano Lett.* **2010**, *10*, 4952−4955.
(25) Gopalakrishnan, A.; Chirumamilla, M.; De Angelis, F.; Toma, A.; Zaccaria, R. P.; Krahne, R. Bimetallic 3D Nanostar Dimers in Ring Cavities: Recyclable and Robust Surface-Enhanced Raman Scattering Substrates for Signal Detection from Few Molecules. *ACS Nano* **2014**, *8*, 7986−7994.
(26) Ameling, R.; Langguth, L.; Hentschel, M.; Mesch, M.; Braun, P. V.; Giessen, H. Cavity-Enhanced Localized Plasmon Resonance Sensing. *Appl. Phys. Lett.* **2010**, *97*, 253116.
(27) Dmitriev, A.; Hägglund, C.; Chen, S.; Fredriksson, H.; Pakizeh, T.; Käll, M.; Sutherland, D. S. Enhanced Nanoplasmonic Optical Sensors with Reduced Substrate Effect. *Nano Lett.* **2008**, *8*, 3893−3898.
(28) Otte, M. A.; Estévez, M.-C.; Carrascosa, L. G.; González-Guerrero, A. B.; Lechuga, L. M.; Sepúlveda, B. Improved Biosensing Capability with Novel Suspended Nanodisks. *J. Phys. Chem. C* **2011**, *115*, 5344−5351.
(29) Shen, Y.; Zhou, J.; Liu, T.; Tao, Y.; Jiang, R.; Liu, M.; Xiao, G.; Zhu, J.; Zhou, Z.-K.; Wang, X.; Jin, C.; Wang, J. Plasmonic Gold Mushroom Arrays with Refractive Index Sensing Figures of Merit Approaching the Theoretical Limit. *Nat. Commun.* **2013**, *4*, 1−9.
(30) Roxworthy, B. J.; Bhuiya, A. M.; Yu, X.; Chow, E. K. C.; Toussaint, K. C., Jr. Reconfigurable Nanoantennas Using Electron-Beam Manipulation. *Nat. Commun.* **2014**, *5*, 1−7.
(31) Neubrech, F.; Beck, S.; Glaser, T.; Hentschel, M.; Giessen, H.; Pucci, A. Spatial Extent of Plasmonic Enhancement of Vibrational Signals in the Infrared. *ACS Nano* **2014**, *8*, 6250−6258.
(32) Dvoynenko, M.; Goncharenko, A.; Romaniuk, V.; Venger, E. Effects of Dimension on Optical Transmittance of Semicontinuous Gold Films. *Phys. B (Amsterdam, Neth.)* **2001**, *299*, 88−93.
(33) Neubrech, F.; Kolb, T.; Lovrincic, R.; Fahsold, G.; Pucci, A.; Aizpurua, J.; Cornelius, T. W.; Toimil-Molares, M. E.; Neumann, R.; Karim, S. Resonances of Individual Metal Nanowires in the Infrared. *Appl. Phys. Lett.* **2006**, *89*, 253104.
(34) Neubrech, F.; Weber, D.; Enders, D.; Nagao, T.; Pucci, A. Antenna Sensing of Surface Phonon Polaritons. *J. Phys. Chem. C* **2010**, *114*, 7299−7301.

DOI: 10.1021/ph500374r
ACS Photonics 2015, 2, 497−505

(35) Cottam, M. G.; Tilley, D. R. *Introduction to Surface and Superlattice Excitations*; Cambridge University Press, 1989; Cambridge Books Online.
(36) Kliewer, K. L.; Fuchs, R. Optical Modes of Vibration in an Ionic Crystal Slab Including Retardation. I. Nonradiative Region. *Phys. Rev.* **1966**, *144*, 495−503.
(37) Kliewer, K. L.; Fuchs, R. Optical Modes of Vibration in an Ionic Crystal Slab Including Retardation. II. Radiative Region. *Phys. Rev.* **1966**, *150*, 573−588.
(38) Neubrech, F.; Pucci, A. Plasmonic Enhancement of Vibrational Excitations in the Infrared. *IEEE J. Sel. Top. Quantum Electron.* **2013**, *19*, 4600809.
(39) Alonso-González, P.; Albella, P.; Neubrech, F.; Huck, C.; Chen, J.; Golmar, F.; Casanova, F.; Hueso, L. E.; Pucci, A.; Aizpurua, J.; Hillenbrand, R. Experimental Verification of the Spectral Shift between Near- and Far-Field Peak Intensities of Plasmonic Infrared Nanoantennas. *Phys. Rev. Lett.* **2013**, *110*, 203902.
(40) Zuloaga, J.; Nordlander, P. On the Energy Shift between Near-Field and Far-Field Peak Intensities in Localized Plasmon Systems. *Nano Lett.* **2011**, *11*, 1280−1283.
(41) Eilers, P. H. C. A Perfect Smoother. *Anal. Chem.* **2003**, *75*, 3631−3636.
(42) Enders, D.; Pucci, A. Surface Enhanced Infrared Absorption of Octadecanethiol on Wet-Chemically Prepared Au Nanoparticle Films. *Appl. Phys. Lett.* **2006**, *88*, 184104.
(43) Porter, M. D.; Bright, T. B.; Allara, D. L.; Chidsey, C. E. D. Spontaneously Organized Molecular Assemblies. 4. Structural Characterization of n-Alkyl Thiol Monolayers on Gold by Optical Ellipsometry, Infrared Spectroscopy, and Electrochemistry. *J. Am. Chem. Soc.* **1987**, *109*, 3559−3568.
(44) Trollmann, J.; Pucci, A. Infrared Dielectric Function of Gold Films in Relation to Their Morphology. *J. Phys. Chem. C* **2014**, *118*, 15011−15018.

DOI: 10.1021/ph500374r
ACS Photonics 2015, 2, 497−505